ICCFD13-2026-308

Shocklet-Capturing Spatial Artificial Neural Network Model for Large Eddy Simulation of Compressible Isotropic Turbulence

Jiahao Zhang*, Qi Dai* and Xiang Wang*
* National Key Laboratory of Transient Physics, Nanjing University of Science and Technology,
Nanjing 210094, China.

Abstract: To address the issues of inaccurate dissipation and insufficient robustness of traditional subgrid-scale (SGS) models in large eddy simulation (LES) of highly compressible turbulence dominated by shocklets, a Shocklet-Capturing Spatial Artificial Neural Network (SCSANN) model is proposed in this paper. Based on high-fidelity direct numerical simulation (DNS) data of compressible isotropic decaying turbulence with an initial turbulent Mach number $M_t = 1.2$, we systematically design multi-dimensional input features that integrate first-order physical basis tensors, second-order spatial derivatives, and a seven-point spatial stencil. *A priori* tests demonstrate that the SCSANN model can accurately reconstruct the SGS stress and heat flux with exceedingly high correlation coefficients and low relative errors. Furthermore, *a posteriori* LES tests verify the model's excellent generalization capability and long-term computational stability under unseen turbulent evolution states. Compared with the dynamic Smagorinsky model (DSM) and the no-model implicit LES, the SCSANN is capable of reproducing the energy cascade process of the flow field with high fidelity. This study provides an effective data-driven paradigm for high-precision SGS modelling in highly compressible turbulent environments.

Keywords: Computational fluid dynamics; large eddy simulation; subgrid-scale model; artificial neural network; highly compressible turbulence; shocklets

1. Introduction

Turbulence is the most common fundamental state of fluid motion. Due to its spatiotemporally random, multiscale, and highly nonlinear characteristics, it is also one of the most complex physical phenomena in engineering applications and nature [1]. When the Mach number of the flow is high, compressibility effects become significant, rendering the turbulence even more complex [2]. Numerical simulation of turbulence mainly relies on three fundamental frameworks: direct numerical simulation (DNS), Reynolds-averaged Navier-Stokes (RANS) methods, and large eddy simulation (LES) [3]. By directly solving the full Navier-Stokes equations, DNS can resolve all spatiotemporal fluctuations from the energy-containing large scales down to the Kolmogorov dissipation scales, providing the most accurate flow field details. However, its computational resource consumption increases dramatically with a power of the Reynolds number, making it difficult to apply directly to practical problems at the current stage. In contrast, the RANS method only solves for the time- or ensemble-averaged field, fully modelling the effects of turbulent fluctuations at all scales. Although RANS is computationally highly efficient, it often struggles to guarantee predictive accuracy when dealing with strongly unsteady flows, large-scale separations, and complex shock-turbulence interactions. Large eddy simulation (LES) achieves an ideal balance between computational cost and physical fidelity by directly resolving large-scale turbulent motions and modelling the subgrid-scale (SGS) fluctuations [4, 5]. Its predictive quality fundamentally depends on the accuracy of the SGS model.

Over the past few decades, researchers have proposed various SGS models. Pure eddy-viscosity models, represented by the Smagorinsky model (SM), the dynamic SM, and the WALE model, are the most widely used. Based on the eddy-viscosity hypothesis and scale-similarity assumptions, they provide reasonable energy dissipation for the system and exhibit extremely high numerical robustness [5]. On the other hand, gradient models based on Taylor series expansions are derived purely from mathematical deduction, demonstrating excellent capabilities in capturing the local stress tensor topology and naturally reflecting the energy backscatter mechanism in turbulence [6]. The dynamic nonlinear model (DNM) combines the robustness of the DSM with the local stress topology-capturing capability of the gradient model, serving as a model that features both stability and accuracy [7]. However, when the flow is highly compressible, particularly when the turbulent Mach number $M_t > 0.3$, the limitations of these traditional models are significantly amplified. At this point, numerous local shocklets spontaneously form in the flow field, accompanied by strong thermodynamic-kinematic coupling effects [8]. Faced with intense expansion/compression effects and complex shock-turbulence interactions, models based on the eddy-viscosity hypothesis often smooth out shock structures in LES due to excessive dissipation [9]. Gradient models frequently lead to numerical divergence due to insufficient robustness [4]. Meanwhile, because the strong discontinuity of shocks simultaneously breaks the smoothness foundation of Taylor expansions and the scale-similarity assumption of dynamic procedures, mixed models are also prone to falling into the dual dilemma of numerical divergence and inaccurate dissipation.

To overcome the limitations of traditional models, deep learning techniques have recently demonstrated tremendous potential and broad application prospects in the field of SGS modelling for LES [10]. By training on high-fidelity DNS data, machine learning algorithms such as neural networks can reconstruct unresolved SGS terms with high accuracy. Xie et al. combined artificial neural networks with the Smagorinsky model and the gradient model to construct an artificial neural network mixed model (ANNMM), balancing the robustness of traditional models with the accuracy of neural networks [11]. Xie et al. also designed multi-point stencil input features to capture the spatial correlation of SGS stresses [12]. Yang et al. selected a linear eddy-viscosity term and a nonlinear term, which are mutually orthogonal, as input features for an artificial neural network based on the SGS stress basis tensor expansion theorem proposed by Silvis [13], thereby endowing the model with good robustness [14]. Frezat et al. explicitly embedded physical prior constraints, such as Galilean invariance and scalar linearity, into a convolutional neural network architecture, improving the numerical stability of *a posteriori* simulations and achieving generalization to unseen operating conditions [15]. Cho et al. proposed a novel recursive training procedure that breaks the bottleneck of lacking high-fidelity training data for high-Reynolds-number LES by using a "low-Reynolds-number DNS data initiation + generative LES data self-iteration" approach. Combined with a dual neural network architecture and strict bias-free physical constraints, this model not only maintained high accuracy at extremely high Reynolds numbers but also successfully achieved perfect generalization to completely unseen decaying turbulence conditions [16].

However, existing SGS models are mostly limited to incompressible or weakly compressible flows. When the flow is highly compressible and shock-dominated, abundant shocklet structures exist in the flow field. Current models often fail to effectively characterize such complex cross-scale energy transfer and compression-expansion mechanisms, thereby losing accuracy and generalization capability.

Aiming at the SGS modelling problem in highly compressible turbulence, this paper constructs a shocklet-capturing spatial artificial neural network (SCSANN) model. We have carefully designed the input features of the model. In *a priori* tests, the SCSANN model demonstrates accurate predictions of SGS stress and heat flux; in *a posteriori* tests, the SCSANN model can adapt to unseen turbulent Mach numbers in LES. In section 2, we briefly introduce the governing equations and numerical methods. In section 3, we introduce the compressible isotropic decaying turbulence DNS database. In section 4, we propose the SCSANN model and detail the input features. In section 5, we present the results of the *a priori* and *a posteriori* tests. In section 6, we draw our conclusions.

2. Numerical Methods

The fundamental concept of large eddy simulation (LES) is to decompose the flow field variables into resolved-scale components, which can be captured by the computational grid, and unresolved subgrid-scale (SGS) components via a low-pass filtering operation. For compressible flows, density-weighted Favre filtering is typically employed to simplify the equation forms. For any spatial physical quantity f, its standard spatial filtering operator is denoted as $\bar{f}$, and the corresponding Favre filter is defined as $\tilde{f} = \overline{\rho f}/\bar{\rho}$, where ρ is the fluid density.

This paper focuses on the study of compressible isotropic decaying turbulence. Neglecting external body forces and external heat sources, the non-dimensionalized compressible filtered full Navier-Stokes (N-S) equations can be expressed as:

$$\frac{\partial \bar{\rho}}{\partial t} + \frac{\partial(\bar{\rho}\tilde{u}_j)}{\partial x_j} = 0, \tag{1}$$

$$\frac{\partial(\bar{\rho}\tilde{u}_i)}{\partial t} + \frac{\partial(\bar{\rho}\tilde{u}_i\tilde{u}_j + \bar{p}\delta_{ij})}{\partial x_j} - \frac{1}{Re}\frac{\partial \tilde{\sigma}_{ij}}{\partial x_j} = -\frac{\partial \tau_{ij}}{\partial x_j} + \frac{1}{Re}\frac{\partial(\bar{\sigma}_{ij} - \tilde{\sigma}_{ij})}{\partial x_j}, \tag{2}$$

$$\frac{\partial \tilde{E}}{\partial t} + \frac{\partial[(\tilde{E} + \bar{p})\tilde{u}_j]}{\partial x_j} - \frac{1}{Re}\frac{\partial(\tilde{\sigma}_{ij}\tilde{u}_i)}{\partial x_j} - \frac{1}{\alpha}\frac{\partial}{\partial x_j}\left(\tilde{\kappa}\frac{\partial \tilde{T}}{\partial x_j}\right) = R_\varepsilon, \tag{3}$$

$$R_\varepsilon = -\frac{\partial(\tau_{ij}\tilde{u}_i)}{\partial x_j} - \frac{1}{(\gamma-1)\gamma M^2}\frac{\partial q_j}{\partial x_j} - \frac{\partial \Pi_j}{\partial x_j} + \frac{1}{Re}\frac{\partial}{\partial x_j}\left(\overline{\sigma_{ij}u_i} - \tilde{\sigma}_{ij}\tilde{u}_i\right) + \frac{1}{\alpha}\frac{\partial}{\partial x_j}\left(\overline{\kappa\frac{\partial T}{\partial x_j}} - \tilde{\kappa}\frac{\partial \tilde{T}}{\partial x_j}\right) \tag{4}$$

In the above equations, t is time, and x_i represents the Cartesian spatial coordinates (using Einstein summation convention); u_i, p, and T denote the fluid velocity components, pressure, and temperature, respectively; δ_{ij} is the Kronecker delta. The dimensionless parameters Re, M, and γ represent the reference Reynolds number, reference Mach number, and specific heat ratio of the gas, respectively, while α is the dimensionless heat conduction parameter. The ideal gas equation of state is adopted:

$$\bar{p} = \frac{\bar{\rho}\tilde{T}}{\gamma M^2}. \tag{5}$$

The resolved-scale total energy $\tilde{E}$ in the energy equation consists of the filtered internal energy and the resolved-scale kinetic energy. For an ideal gas, it is defined as:

$$\tilde{E} = \bar{\rho}\tilde{e} + \frac{1}{2}\bar{\rho}\tilde{u}_i\tilde{u}_i = \frac{\bar{p}}{\gamma - 1} + \frac{1}{2}\bar{\rho}\tilde{u}_k\tilde{u}_k. \tag{6}$$

The constitutive relations for the large-scale flow field depend on the resolved-scale variables. The Favre-filtered strain rate tensor is defined as $\tilde{S}_{ij} = \frac{1}{2}(\partial\tilde{u}_i/\partial x_j + \partial\tilde{u}_j/\partial x_i)$. Based on the large-scale temperature field $\tilde{T}$ and combined with Sutherland's law, the filtered viscosity coefficient $\tilde{\mu}$ and thermal conductivity $\tilde{\kappa}$ can be calculated, which in turn yield the resolved-scale viscous stress tensor:

$$\tilde{\sigma}_{ij} = 2\tilde{\mu}\tilde{S}_{ij} - \frac{2}{3}\tilde{\mu}\delta_{ij}\tilde{S}_{kk}. \tag{7}$$

The filtering operation inevitably truncates small-scale information, thereby introducing unclosed SGS terms on the right-hand sides of the momentum and energy equations. These unclosed terms primarily include the SGS stress tensor τ_{ij}, the SGS heat flux q_j, and the SGS pressure-velocity work Π_j, whose mathematical definitions are as follows:

$$\tau_{ij} = \overline{\rho u_i u_j} - \bar{\rho}\tilde{u}_i\tilde{u}_j, \quad q_j = \overline{\rho u_j T} - \bar{\rho}\tilde{u}_j\tilde{T}, \quad \Pi_j = \overline{p u_j} - \bar{p}\tilde{u}_j \tag{8}$$

In the LES of compressible fluids, the SGS stress τ_{ij} and SGS heat flux q_j dominate the cross-scale momentum transfer and energy transport, serving as the most critical SGS terms in the governing equations. To effectively close these terms, scholars have proposed various SGS models, with the dynamic Smagorinsky model (DSM) and the gradient model (GM) being the most representative. The core idea of the DSM is to dynamically and locally "compute" model coefficients using the known large-scale resolved information in the flow field. Its theoretical foundation relies on the double-filtering technique: on top of the original grid filter (filter width $\bar{\Delta}$), a test filter with a scale $\hat{\Delta}$ (typically $\hat{\Delta} = 2\bar{\Delta}$) is introduced. According to the Germano identity, a strict mathematical correlation exists between the SGS stresses at the grid scale and the test scale, thereby allowing the exact calculation of the resolved Leonard stress $L_{ij} = \widehat{\tilde{u}_i\tilde{u}_j} - \hat{\tilde{u}}_i\hat{\tilde{u}}_j$. Combined with the Smagorinsky eddy-viscosity assumption, Lilly proposed using the least squares method to minimize the sum of squared errors, consequently obtaining the dynamic coefficients C_R and C_T for the SGS stress and heat flux:

$$C_R = \frac{L^*_{ij}M_{ij}}{M_{kl}M_{kl}}, \quad C_T = \frac{H_j N_j}{N_k N_k} \tag{9}$$

In the equations above, L^*_{ij} is the anisotropic part of the Leonard stress, while M_{ij} and N_j are functions of the strain rate tensor and temperature gradient at both the test scale and the grid scale, respectively. Distinct from the DSM which introduces an eddy-viscosity assumption, the GM is derived based on the Taylor series expansion of the filtering convolution integral. For a box filter, its leading-order terms can express the SGS stress and heat flux as nonlinear combinations of the gradients of the resolved-scale variables. For instance, its stress term can be approximated as:

$$\tau_{ij}^{GM} = \frac{\bar{\Delta}^2}{12}\bar{\rho}\frac{\partial \tilde{u}_i}{\partial x_k}\frac{\partial \tilde{u}_j}{\partial x_k} \tag{10}$$

However, in highly compressible isotropic turbulence, the flow field is accompanied by an abundance of shocklets, rendering traditional SGS models ineffective. The SCSANN model trained in this paper will be used to predict the SGS stress τ_{ij} and SGS heat flux q_j in highly compressible isotropic turbulence.

The spatial discretization scheme for the convective terms in the solver adopts a seventh-order WENO-Z scheme [17, 18]. By introducing a global high-order smoothness indicator to optimize the allocation mechanism of nonlinear weights, this scheme not only robustly captures complex shocklet structures in highly compressible turbulence but also minimizes numerical dissipation in smooth regions.

Both the DNS and *a posteriori* LES in this study rely on the open-source compressible fluid dynamics solver PeleC [19], which is capable of computing compressible isotropic turbulence and possesses good accuracy for turbulent energy spectra [20] as well as shock-capturing capabilities [21]. Furthermore, to meet the requirements of *a posteriori* solving with the SGS model constructed in this study, we conducted targeted secondary development on the source code of PeleC.

3. DNS Database of Compressible Isotropic Decaying Turbulence

The dataset used to train the model in this paper is derived from DNS data of compressible isotropic decaying turbulence. The turbulent Mach number M_t and Taylor Reynolds number Re_λ are defined as:

$$M_t = M\frac{u^{rms}}{\langle\sqrt{T}\rangle}, Re_\lambda = Re\frac{\langle\rho\rangle u^{rms}\lambda}{\sqrt{3}\langle\mu\rangle}, \tag{11}$$

where $\langle\cdot\rangle$ denotes spatial averaging. The root-mean-square (rms) value of velocity is defined as $u^{rms} = \sqrt{\langle u_i u_i \rangle}$, and the Taylor microscale λ is defined as:

$$\lambda = \sqrt{\frac{\langle u_i u_i \rangle}{\langle (\partial u_1/\partial x_1)^2 + (\partial u_2/\partial x_2)^2 + (\partial u_3/\partial x_3)^2 \rangle}}. \tag{12}$$

The Kolmogorov scale η and the integral scale L_I are defined respectively as:

$$\eta = [\langle \mu/(Re\rho) \rangle^3/\epsilon]^{1/4}, \quad L_I = \frac{3\pi}{2(u^{rms})^2}\int_0^\infty \frac{E(k)}{k}dk, \tag{13}$$

where ϵ is the spatial average of the dissipation rate per unit mass, $\epsilon = \langle \sigma_{ij} S_{ij}/(Re\rho) \rangle$, and $E(k)$ is the kinetic energy spectrum per unit mass such that $\int_0^\infty E(k)dk = (u^{rms})^2/2$. The initial flow field is generated in Fourier space according to the Passot-Pouquet spectrum:

$$E_0(k) = Ak^4 e^{-2k^2/k_0^2} \tag{14}$$

where k is the wavenumber, $k_0 = 4$ is the peak wavenumber, and $A = 4.3 \times 10^{-4}$. All initial thermodynamic variables are set to constant values and normalized to 1.

The initial turbulent Mach number is set to $M_{t0} = 1.2$, and the initial Taylor Reynolds number is $Re_{\lambda 0} = 120$. The number of grid cells in the computational domain is 256^3, and the relevant scale parameters satisfy $k_{max}\eta \approx 2.91$, where k_{max} is the maximum wavenumber and η is the Kolmogorov scale. The ratio of the integral scale to the Kolmogorov scale is $L_I/\eta \approx 27.53$, and the Taylor microscale ratio is $\lambda/\eta \approx 21.29$, ensuring physical resolution across the full range of scales. Defining the large-eddy turnover time as $\tau_{et} = \frac{L_I}{u^{rms}}$, we simulated the isotropic decaying turbulence for a total of $5\tau_{et}$. The velocity spectra for DNS and fDNS at $t = \tau_{et}$ are shown in figure 1. A standard three-dimensional Gaussian filter is applied to filter the DNS data, with the filter function given by:

$$G(\boldsymbol{r}) = \left(\frac{6}{\pi\Delta^2}\right)^{1.5} \exp\left(-\frac{6\boldsymbol{r}\cdot\boldsymbol{r}}{\Delta^2}\right), \tag{15}$$

In this study, the filter width is set to $\Delta = 4\Delta_{DNS}$. Because the initial field is generated according to the Passot-Pouquet spectrum, $k = 4$ remains the peak wavenumber. At this point, the unphysical effects of the artificial initial field dissipate, and the flow field enters a self-similar evolution phase, satisfying the $-5/3$ power law in the inertial subrange.

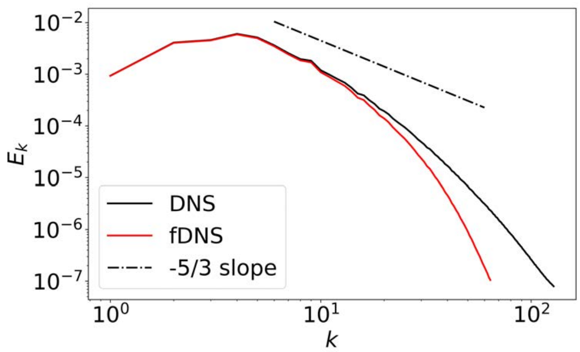

Figure 1: Spectrum of velocity for DNS and fDNS at $t = \tau_{et}$

Both the training and validation sets are sampled from the DNS data within the range $t \in (\tau_{et}, 5\tau_{et})$, where 80% of the samples are used as the training set and 20% as the validation set. The role of the validation set is to monitor the training progress of the model in real time and save the optimal model based on its performance on the validation set. When constructing the datasets, all input features and training labels for the model are calculated from the filtered DNS fields.

4. Shocklet-Capturing Spatial Artificial Neural Network

4.1 Network Architecture

Current common architectures for neural network SGS models include multi-layer perceptrons (MLP), convolutional neural networks (CNN), and graph neural networks (GNN). In this study, a Shocklet-Capturing Spatial Artificial Neural Network (SCSANN) model is constructed using an MLP architecture to establish the nonlinear mapping relationship between the Favre-filtered variables and the unclosed SGS terms. Since we are investigating the SGS modelling of isotropic turbulence at $M_t = 1.2$, an abundance of shocklets exists in the flow field, leading to discontinuities in the SGS stress and heat flux fields. The multi-layer convolution operations of CNNs would introduce smoothing effects, thereby washing out sharp gradients, whereas MLPs can better preserve these discontinuous structures. The MLP architecture is illustrated in figure 2, and this nonlinear relationship can be expressed as:

$$h^{(n)} = g(W^{(n)}h^{(n-1)} + b^{(n)}) \tag{16}$$

where $W^{(n)}$ and $b^{(n)}$ represent the weight matrix and bias vector of the n-th layer, respectively, $h^{(n-1)}$ is the output of the $(n-1)$-th layer, and g is the nonlinear activation function. In this study, SCSANN consists of 7 hidden layers, adopting an "expand-then-narrow" design, with the number of neurons sequentially set to 512, 1024, 2048, 512, 128, 64, and 32.

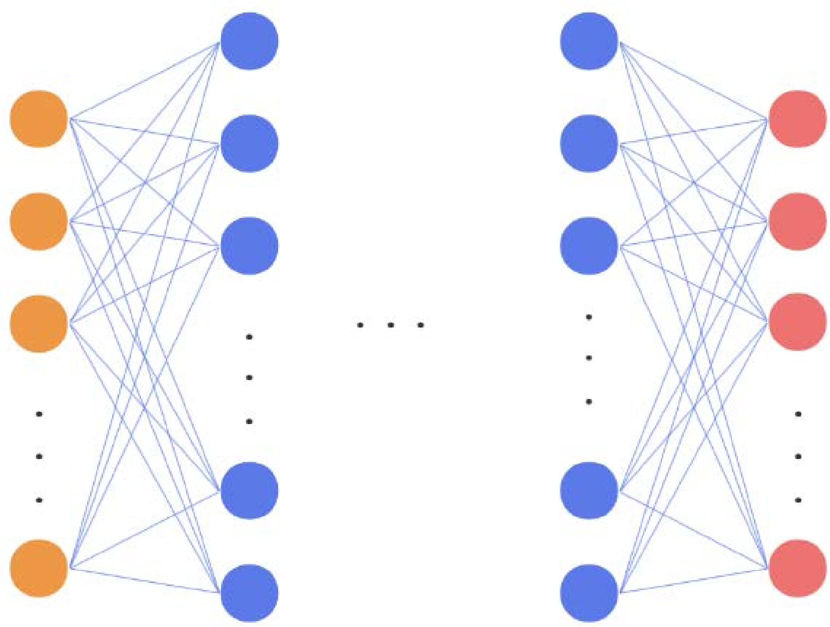

Figure 2: Schematic diagram of the multi-layer perceptron (MLP) architecture.

During the model training process, a backpropagation algorithm is used to optimize the weights and biases to minimize the loss function. Due to the presence of numerous shocklet structures in the flow field, the SGS terms take on very large values near shocks and very small values in smooth regions, resulting in an extremely wide span of data scales in the training set. Therefore, this paper employs a relative L_2 loss function, defined as:

$$\mathcal{L} = \frac{1}{N}\sum_{i=1}^{N}\frac{(\hat{y}_i - y_i)^2}{y_i^2 + \epsilon^2} \tag{17}$$

where $\hat{y}_i$ is the predicted value of the model, y_i is the corresponding true label value, ϵ is an infinitesimally small constant to prevent division by zero, and N is the number of samples in the training set. This loss function normalizes errors across different scales; regardless of whether a sample lies in a large-value interval or a small-value interval, a prediction deviation of the same proportion will yield a calculated loss of the same order of magnitude. Since there are many values near zero in the training set, this paper adopts the GELU activation function. Compared to the traditional ReLU, the GELU function approaches zero more smoothly for small values without hard truncation, making the network more sensitive to inputs near zero. To enhance the robustness during model training, all input features and output labels are standardized by their rms values, namely $Z_{input} = X_{input}/X_{input}^{rms}$ and $Z_{output} = X_{output}/X_{output}^{rms}$, where X_{input}^{rms} and X_{output}^{rms} are the rms values of the input and output variables, respectively. This paper uses the Adam optimizer and a cosine annealing learning rate scheduling strategy.

4.2 Input Features

Accurately reconstructing SGS terms in highly compressible flow fields requires carefully selecting the input features for the neural network. On one hand, due to the abundance of shocklets and complex thermodynamic-kinematic coupling in the flow field, the input features should provide ample spatial information; on the other hand, since neural networks are relatively sensitive to input features, the features should conform to the physical relationships of the SGS terms. Based on the basis tensor representation theorem for SGS stress and the basis vector representation theorem for SGS heat flux, this paper selects first-order input features. Considering the non-local nature of SGS terms in highly compressible flow fields, second-order derivatives and a seven-point spatial stencil are also introduced.

It is generally accepted that the SGS stress tensor can be expressed as a nonlinear function of the filtered strain rate tensor and the filtered rotation rate tensor [22, 23], while the SGS heat flux can be expressed as a nonlinear function of the filtered temperature gradient, the filtered strain rate tensor, and the filtered rotation rate tensor [24]:

$$\tau_{ij} = f\left(\tilde{S}_{ij}, \tilde{\Omega}_{ij}, \delta_{ij}\right) \tag{18}$$

$$q_i = f\left(\frac{\partial \widetilde{T}}{\partial x_i}, \tilde{S}_{ij}, \tilde{\Omega}_{ij}, \delta_{ij}\right). \tag{19}$$

Based on the representation theorem for isotropic functions, combined with dimensional analysis and tensor invariant theory, scholars [25, 26] further proposed simplified expressions for equations 18 and 19:

$$\tau_{ij} = \sum_{k=0}^{m} \alpha_k T_{ij}^k, \tag{20}$$

$$q_i = \sum_{k=1}^{n} \beta_k V_i^k, \tag{21}$$

where α_k and β_k are model coefficients, and T_{ij}^k and V_i^k are basis tensors. From a mathematical perspective, the SGS stress and SGS heat flux should be expanded according to the basis tensors given in equations 20 and 21. However, this would make the expressions too complicated for practical application. Therefore, in this paper, we select suitable basis tensors from equations 20 and 21 as input features for SCSANN. In LES, the filtered strain rate tensor $T_{ij}^1 = S_{ij}$ is directly related to the SGS kinetic energy production term $P_{sgs} = -\tau_{ij}S_{ij}$, dominating the linear eddy-viscosity dissipation of turbulence; thus, the strain rate tensor is selected as the first input feature. Extensive *a priori* studies have shown that the true SGS stress tensor is generally not collinear with the strain rate tensor, making it necessary to select a basis tensor orthogonal to the strain rate tensor S_{ij}. $T_{ij}^4 = S\Omega - \Omega S$ is the simplest basis tensor strictly orthogonal to S_{ij}; it does not directly contribute to the macroscopic dissipation of energy but can effectively characterize the complex non-dissipative phenomena induced by the coupling of flow field rotation and stretching, including energy backscatter. Hence, it is chosen as the second input feature. The filtered temperature gradient $V_i^1 = \frac{\partial \widetilde{T}}{\partial x_i}$ describes the diffusive behaviour of heat following the second law of thermodynamics and is selected as the third input feature. In genuine compressible turbulence, strong thermodynamic-kinematic coupling exists in the flow field, and the true SGS heat flux is generally not collinear with the temperature gradient. We select the basis vector orthogonal to the temperature gradient, $V_i^3 = \Omega_{ij}\frac{\partial \widetilde{T}}{\partial x_i}$, as the fourth input feature; it describes the entrainment effect of vortex rotation on heat transfer, endowing the model with the ability to capture non-collinear transport and even local counter-gradient transport.

In highly compressible isotropic turbulence with a turbulent Mach number up to $M_t = 1.2$, numerous shocklets spontaneously generate within the flow field. The severe thermodynamic-kinematic coupling effects impart strong non-local properties to the SGS stress and SGS heat flux. First-order derivative information at a single point (velocity and temperature gradients) is insufficient to reconstruct the SGS terms accurately. Therefore, this study additionally incorporates the second-order derivatives of velocity and temperature into the input features, and designs a 7-point spatial stencil (i.e., the current cell and its 6 adjacent cells in the three Cartesian directions). Let $\mathcal{F}^{(i,j,k)}$ denote the feature set of the current cell:

$$\mathcal{F}^{(i,j,k)} = \left\{ \tilde{S}_{ij}, \tilde{S}_{ik}\tilde{\Omega}_{kj} - \tilde{\Omega}_{ik}\tilde{S}_{kj}, \frac{\partial \tilde{T}}{\partial x_i}, \tilde{\Omega}_{ij}\frac{\partial \tilde{T}}{\partial x_i}, \frac{\partial^2 \tilde{u}_i}{\partial x_p \partial x_q}, \frac{\partial^2 \tilde{T}}{\partial x_p \partial x_q} \right\}^{(i,j,k)}. \tag{22}$$

To evaluate the contributions of different features to the prediction of SGS terms, we designed a total of three sets of input features as listed in table 1, corresponding to the models SCSANN-1, SCSANN-2, and SCSANN-3, respectively. The input features of SCSANN-1 contain only the first-order derivative information of the current grid cell, namely the filtered strain rate tensor $\tilde{S}_{ij}$, the rotation-stretching coupling basis tensor $\tilde{S}_{ik}\tilde{\Omega}_{kj} - \tilde{\Omega}_{ik}\tilde{S}_{kj}$ orthogonal to the strain rate, the filtered temperature gradient $\frac{\partial \tilde{T}}{\partial x_i}$, and the vortex entrainment basis tensor $\tilde{\Omega}_{ij}\frac{\partial \tilde{T}}{\partial x_i}$ orthogonal to the temperature gradient. Based on SCSANN-1, SCSANN-2 further introduces the filtered second-order velocity derivative $\frac{\partial^2 \tilde{u}_i}{\partial x_p \partial x_q}$ and the filtered second-order temperature derivative $\frac{\partial^2 \tilde{T}}{\partial x_p \partial x_q}$ of the current cell. Building upon SCSANN-2, SCSANN-3 additionally incorporates the 7-point spatial stencil (indicated by "spatial"). Figure 3 shows the loss value curves during the training processes of the three models; the training process of SCSANN-3 is the most stable and converges the best. We test the performance of the three models respectively in the subsequent *a priori* tests.

Table 1: Inputs and outputs for different models

Models	Raw inputs	Raw outputs
$SCSANN-1$	$\tilde{S}_{ij}, \tilde{S}_{ik}\tilde{\Omega}_{kj} - \tilde{\Omega}_{ik}\tilde{S}_{kj}, \frac{\partial \tilde{T}}{\partial x_i}, \tilde{\Omega}_{ij}\frac{\partial \tilde{T}}{\partial x_i}$	τ_{ij}, q_i
$SCSANN-2$	$\tilde{S}_{ij}, \tilde{S}_{ik}\tilde{\Omega}_{kj} - \tilde{\Omega}_{ik}\tilde{S}_{kj}, \frac{\partial \tilde{T}}{\partial x_i}, \tilde{\Omega}_{ij}\frac{\partial \tilde{T}}{\partial x_i}, \frac{\partial^2 \tilde{u}_i}{\partial x_p \partial x_q}, \frac{\partial^2 \tilde{T}}{\partial x_p \partial x_q}$	τ_{ij}, q_i
$SCSANN-3$	spatial $(\tilde{S}_{ij}, \tilde{S}_{ik}\tilde{\Omega}_{kj} - \tilde{\Omega}_{ik}\tilde{S}_{kj}, \frac{\partial \tilde{T}}{\partial x_i}, \tilde{\Omega}_{ij}\frac{\partial \tilde{T}}{\partial x_i}, \frac{\partial^2 \tilde{u}_i}{\partial x_p \partial x_q}, \frac{\partial^2 \tilde{T}}{\partial x_p \partial x_q})$	τ_{ij}, q_i

5. Results

In this section, we evaluate the performance of the SCSANN model in both *a priori* and *a posteriori* test phases, comparing the results with the filtered DNS data.

5.1 *A priori* tests

We evaluated the correlation coefficient R and the relative error $E_r = \frac{(\hat{y}-y)_{rms}}{y_{rms}}$ of the three models listed in table 1 (SCSANN-1, SCSANN-2, SCSANN-3) when predicting $\tau_{11}, \tau_{12}, q_1$ on the validation set,

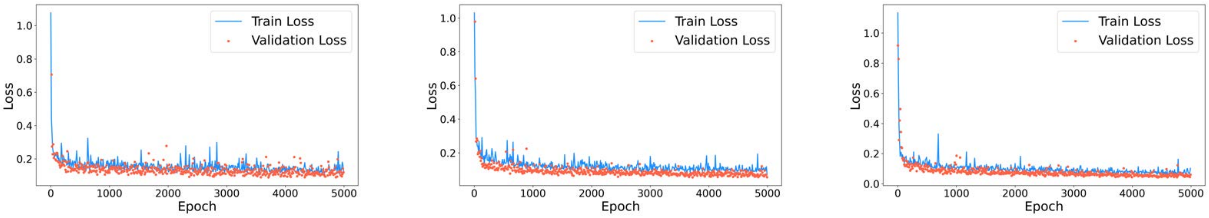

(a) (b) (c)

Figure 3: Evolution of the relative L_2 loss on training and validation sets: (a) SCSANN-1, (b) SCSANN-2, (c) SCSANN-3.

with the results presented in table 2. It can be seen that the SCSANN-1 model, which uses only single-point first-order derivative features, slightly outperforms the GM based on Taylor expansion in predictive performance. However, its improvements in the correlation coefficient and relative error are relatively limited. This is because, in strongly compressible turbulence at $M_t = 1.2$, relying solely on local, linear information is insufficient to accurately establish the mapping between shock-turbulence and the SGS terms. The predictive accuracy of the SCSANN-2 model, which introduces second-order derivatives of velocity and temperature, is significantly improved, with its correlation coefficients R for predicting $\tau_{11}, \tau_{12}, q_1$ comprehensively exceeding 0.96. Simultaneously, the relative error E_r is drastically reduced compared to SCSANN-1, indicating that the local curvature and inflection point information provided by the second-order derivatives can effectively enhance the spatial perception capability of the model. The SCSANN-3 model, utilizing the 7-point spatial stencil, demonstrates the most optimal predictive performance. This indicates that incorporating spatial correlation information from adjacent cells endows the neural network with an implicit "deconvolution" capability, further boosting prediction performance. Consequently, in the subsequent *a priori* and *a posteriori* tests, only SCSANN-3 is used and is referred to simply as SCSANN.

Table 2: Correlation coefficient (R) and relative error (E_r) of τ_{ij} and q_i for different models on the validation set.

R	τ_{11}	τ_{12}	q_1
GM	0.8570	0.8827	0.8502
$SCSANN-1$	0.9278	0.9507	0.9536
$SCSANN-2$	0.9636	0.9770	0.9733
$SCSANN-3$	0.9710	0.9813	0.9771

E_r	τ_{11}	τ_{12}	q_1
GM	0.4136	0.4404	0.5064
$SCSANN-1$	0.2838	0.3121	0.3039
$SCSANN-2$	0.2032	0.2136	0.2362
$SCSANN-3$	0.1813	0.1922	0.2158

We detail the predictive performance metrics of the SCSANN model for SGS stress and SGS heat flux on the validation set, as shown in table 3. The results show that the model achieves precise predictions across all output variables, exhibiting high correlation coefficients R and low relative errors $E_r = \frac{(\hat{y}-y)_{rms}}{y_{rms}}$. Since the model is trained on compressible isotropic decaying turbulence DNS data encompassing flow fields at various turbulent Mach numbers and Taylor Reynolds numbers, the model inherently possesses the potential for cross-Mach-number and cross-Reynolds-number prediction, demonstrating excellent generalization capability and numerical robustness.

Figure 4 displays the spatial contour distributions of the SGS stress τ_{12} and the SGS heat flux q_1 pre-

Table 3: Correlation coefficient (R) and relative error (E_r) of τ_{ij} and q_i for the validation set with the SCSANN.

Validation	τ_{11}	τ_{22}	τ_{33}	τ_{12}	τ_{13}	τ_{23}	q_1	q_2	q_3
R	0.9710	0.9718	0.9722	0.9813	0.9812	0.9817	0.9771	0.9775	0.9778
E_r	0.1813	0.1792	0.1794	0.1922	0.1926	0.1905	0.2158	0.2129	0.2112

dicted by various SGS models at the slice $x = \pi$ (computational domain length is $2\pi^3$) at $t = 2\tau_{et}$. As can be seen from the figure, the SCSANN model exhibits the ability to accurately predict the SGS stress and SGS heat flux within local shocklet regions. Its predicted high-stress bands and extremum regions of heat flux are highly consistent with the filtered DNS (fDNS) fields in terms of spatial location, geometrical topological morphology, and numerical magnitude. Although the gradient model (GM) can reproduce the fundamental topological features of the stress field, it shows significant deviations in the quantitative prediction of its numerical amplitudes. Due to its inherent characteristics of excessive physical dissipation, the dynamic Smagorinsky model (DSM) predicts an overly smooth stress field distribution, severely wiping out the high-stress bands and extremum regions of heat flux generated by shock compression in the true flow field.

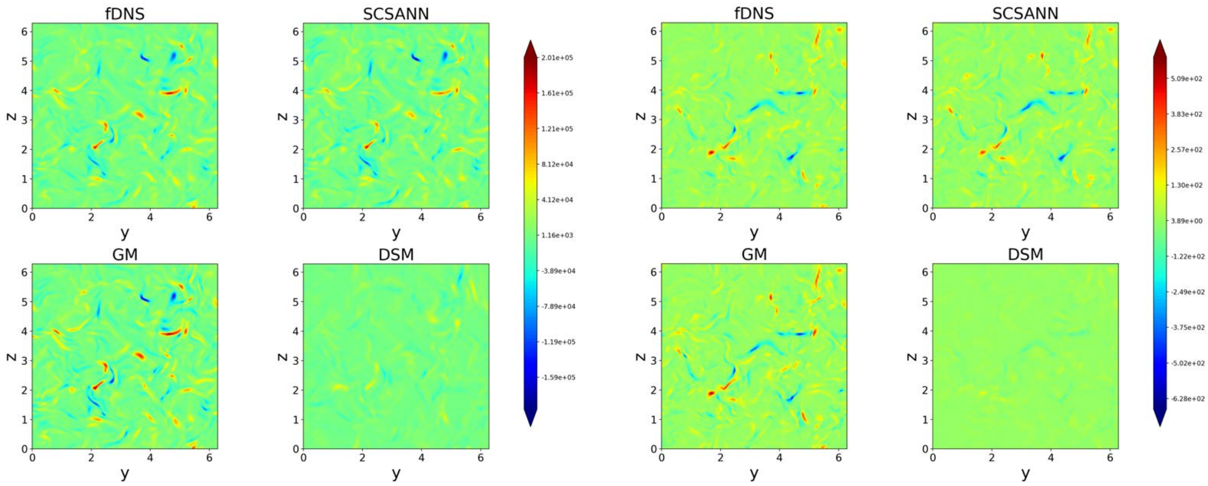

(a) (b)

Figure 4: Contours of SGS terms at the $t = 2\tau_{et}, x = \pi$ slice comparing fDNS, SCSANN, GM, and DSM: (a) SGS stress τ_{12}, (b) SGS heat flux q_1.

5.2 *A posteriori* tests

To further verify the model's performance in actual large eddy simulations, we conducted *a posteriori* tests on SCSANN. We performed LES of compressible isotropic decaying turbulence with an initial turbulent Mach number of $M_t = 1.2$. The computational domain length is $2\pi^3$, the grid resolution is 128^3, and the filter-to-grid ratio (FGR) is set to $\Delta/h_{LES} = 2$, where Δ is the filter width and h_{LES} is the grid spacing. Setting FGR=2 aims to decouple the numerical discretization error from the modelling effect of the SGS model in the wavenumber space, thereby effectively eliminating the interference of numerical errors and ensuring that the discrepancies between the LES and fDNS results originate primarily from the modelling errors of the SGS model.

We also conducted *a posteriori* tests utilizing the DSM and a no-model (implicit LES) configuration separately. The results demonstrate that, in the *a posteriori* phase, the SCSANN can accurately reconstruct the energy cascade, the evolution of vortex structures and shock structures, and the thermodynamic-kinematic coupling, whilst maintaining excellent robustness in long-term computations.

Figure 5 plots the time evolution curves of the resolved turbulent kinetic energy for $t \in (0, 5\tau_{et})$ in the *a posteriori* LES. Due to the lack of external energy injection in compressible isotropic decaying turbulence, the resolved turbulent kinetic energy of the flow field exhibits a monotonically decreasing trend along with the breakdown of large-scale eddies and the energy cascade. When the SCSANN model is enabled, the evolution curve of the resolved turbulent kinetic energy in the LES field closely aligns with that of the fDNS field; the model is able to accurately reconstruct the SGS kinetic energy transport and maintain stability and accuracy during the long-term evolution of the turbulence. When no SGS model is enabled (NO MODEL), the solver is unable to model the physical dissipation at the subgrid scales, and the resolved turbulent kinetic energy remains consistently higher than that of the fDNS field. The DSM exhibits a pronounced feature of excessive dissipation, where the resolved turbulent kinetic energy decays too rapidly, and its evolution curve stays below the fDNS field throughout the entire computational cycle.

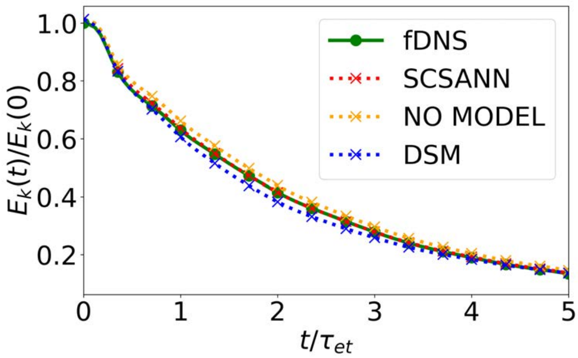

Figure 5: Normalized Resolved Turbulent Kinetic Energy.

We further examined the capability of the SCSANN model to reconstruct the energy spectrum and the kinetic energy cascade in the *a posteriori* phase. Figure 6 compares the velocity spectra of various LES fields and the fDNS field at $t = \tau_{et}, 2\tau_{et}, 3\tau_{et}, 4\tau_{et}$ in the compressible isotropic decaying turbulence with an initial turbulent Mach number of $M_t = 1.2$. The velocity spectrum of the LES field utilizing the SCSANN model highly agrees with the velocity spectrum of the fDNS field across the entire wavenumber range, with only a slight upward curl near the cut-off wavenumber. In the absence of an SGS model (NO MODEL / implicit LES), due to the lack of necessary SGS dissipation, the velocity spectrum of its LES field is higher than that of the fDNS. The DSM, conversely, exhibits excessive dissipation characteristics, dissipating far too much across all wavenumber ranges and leading to a severe attenuation of energy.

It is noteworthy that the compressible isotropic decaying turbulence in the *a posteriori* phase possesses a high degree of non-stationarity, with the turbulent Mach number of the flow field continually changing as the computation proceeds. The SCSANN model only used local data from $t \in (\tau_{et}, 5\tau_{et})$ during the training phase. However, in the *a posteriori* dynamic computation, the model smoothly navigated the severe transient transition period of the high turbulent Mach number initial field evolution from $t \in (0, \tau_{et})$, and maintained exceptionally high predictive accuracy during the subsequent long-term computations.

In compressible isotropic turbulence, the dilatation and compression effects of the flow field are critical physical quantities that characterize the dominant role of shocklet dynamics and acoustic energy. Figure 7 compares the spatial contour distributions of the normalized velocity divergence after one large-eddy turnover time ($t = \tau_{et}$). The LES results based on the SCSANN model show a high degree of topological correlation with the fDNS reference field in space. Under strongly compressible conditions, the SCSANN model accurately captures the complex network features of shocklets induced by vortex stretching and squeezing. Its predicted strong compression bands are highly consistent with the fDNS in terms of geometrical morphology, spatial coherence, and local extremum intensity. By contrast, the dynamic Smagorinsky model (DSM) smoothes out the majority of the shock structures, whilst the no-model formulation (NO MODEL) exhibits unphysical local numerical oscillations. This thoroughly demonstrates that the neural network possesses cross-scale spatial perception capabilities, enabling it to effectively identify

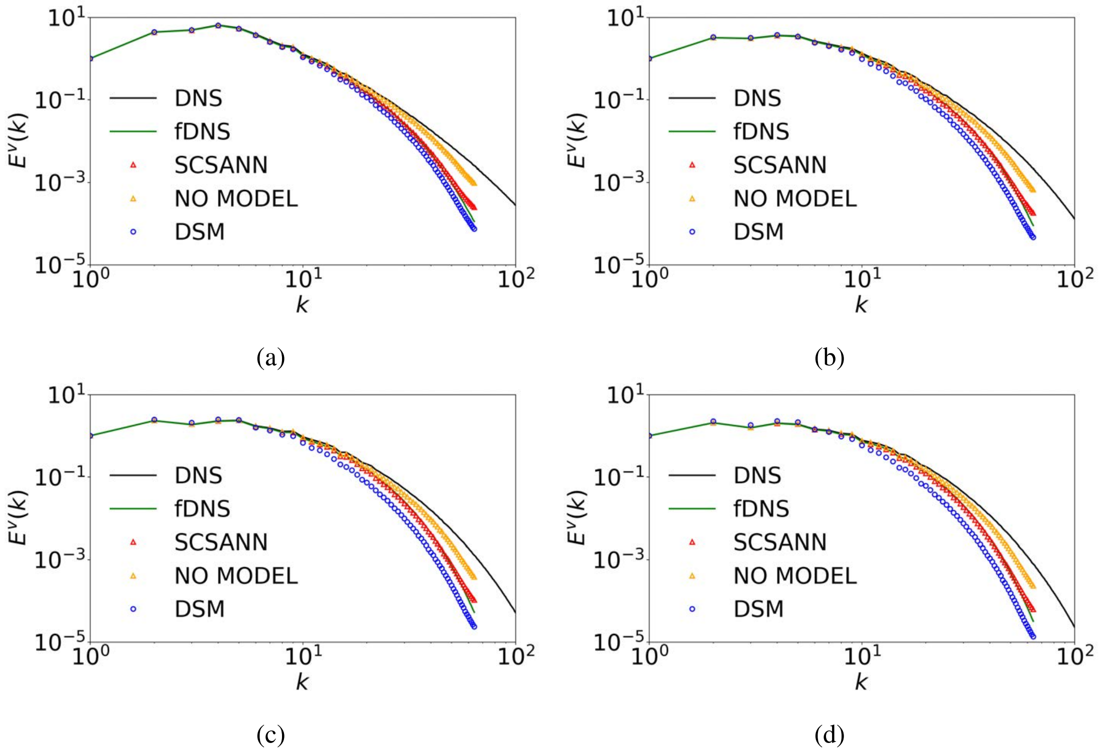

Figure 6: Spectrum of velocity for LES at grid resolutions of $128^3(h^{\Delta}_{LES} = \Delta/2)$ with the filter width $\Delta = 4\Delta x$: (a) $t = \tau_{et}, M_t = 0.93$; (b) $t = 2\tau_{et}, M_t = 0.68$; (c) $t = 3\tau_{et}, M_t = 0.53$; (d) $t = 4\tau_{et}, M_t = 0.43$.

local strong compression effects and accurately impose the corresponding intensity of SGS dissipation.

6. Conclusions

Aiming at the subgrid-scale (SGS) modelling challenges in highly compressible isotropic decaying turbulence (initial $M_t = 1.2$), a novel Shocklet-Capturing Spatial Artificial Neural Network (SCSANN) model is proposed and validated in this paper. At exceedingly high turbulent Mach numbers, the intense shock-turbulence interactions often force traditional eddy-viscosity and mixed models into a dual dilemma of excessive dissipation or numerical divergence. To address this, the present study utilizes a multi-layer perceptron (MLP) framework to successfully construct a high-dimensional nonlinear mapping between the filtered resolved variables and the unclosed SGS terms (SGS stress and heat flux).

Through systematic design and ablation evaluation of the model's input features, we draw the following key conclusions: models relying solely on single-point first-order gradients are insufficient to fully characterize the complexity of highly compressible flows; introducing second-order spatial derivatives of velocity and temperature greatly enhances the model's curvature recognition capability regarding the inflection point features of local shocklet fronts; furthermore, incorporating a seven-point spatial stencil provides the neural network with crucial non-local topological awareness, enabling it to achieve optimal predictive accuracy when reconstructing extreme momentum and heat transport across shock fronts.

A priori test results demonstrate that the SCSANN model achieves an extremely high prediction correlation coefficient ($R > 0.97$) and exceptionally low relative errors on the validation set. The model accurately reconstructs the spatial topological distributions of the SGS stress and heat flux at a physical level.

A posteriori tests further verified the high fidelity and long-term stability of the SCSANN model in actual large eddy simulations. Compared to the dynamic Smagorinsky model (DSM), which exhibits severe

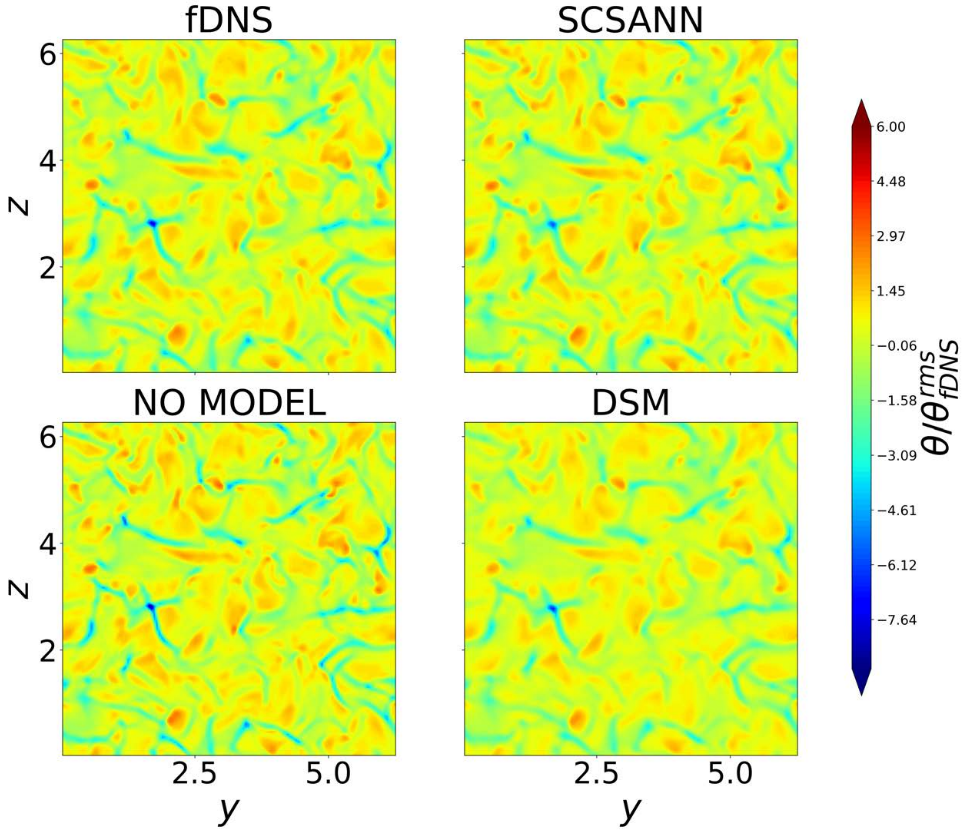

Figure 7: Contours of the normalized velocity divergence $\theta/\theta^{rms}_{fDNS}$ on an arbitrarily selected y-z slice at $t/\tau_{et} = 1$, comparing fDNS, SCSANN, NO MODEL, and DSM.

unphysical over-smoothing effects, and the NO MODEL formulation, which is prone to generating unphysical energy pile-up at the cut-off wavenumber, the SCSANN achieves substantial advantages. It successfully models the energy cascade process. More importantly, the SCSANN achieves a stringent reproduction of the resolved-scale turbulent kinetic energy decay inherent to the native DNS system within the LES framework.

In summary, the SCSANN model effectively overcomes the theoretical bottlenecks of traditional SGS models when handling highly compressible flows, achieving an ideal balance between numerical stability and fluid dynamic fidelity.

Acknowledgements

This work was supported by the Postgraduate Research & Practice Innovation Program of Jiangsu Province (Grant No. KYCX25_0805).

References

[1] Stewart Cant. Sb pope, turbulent flows, cambridge university press, cambridge, uk, 2000, 771 pp. *Combustion and Flame*, 125(4):1361–1362, 2001.

[2] Sanjiva K Lele. Compressibility effects on turbulence. *Annual review of fluid mechanics*, 26(1):211–254, 1994.

[3] Philippe R Spalart. Strategies for turbulence modelling and simulations. *International journal of heat and fluid flow*, 21(3):252–263, 2000.

[4] Eric Garnier, Nikolaus Adams, and Pierre Sagaut. *Large eddy simulation for compressible flows*.

Springer Science & Business Media, 2009.

[5] Charles Meneveau and Joseph Katz. Scale-invariance and turbulence models for large-eddy simulation. *Annual Review of Fluid Mechanics*, 32(1):1–32, 2000.

[6] Pierre Sagaut. *Large eddy simulation for incompressible flows: an introduction*. Springer, 2006.

[7] Bing-Chen Wang and Donald J Bergstrom. A dynamic nonlinear subgrid-scale stress model. *Physics of Fluids*, 17(3), 2005.

[8] Sangsan Lee, Sanjiva K Lele, and Parviz Moin. Eddy shocklets in decaying compressible turbulence. *Physics of Fluids A: Fluid Dynamics*, 3(4):657–664, 1991.

[9] M Pino Martín, Ugo Piomelli, and Graham V Candler. Subgrid-scale models for compressible large-eddy simulations. *Theoretical and Computational Fluid Dynamics*, 13(5):361–376, 2000.

[10] Steven L Brunton, Bernd R Noack, and Petros Koumoutsakos. Machine learning for fluid mechanics. *Annual review of fluid mechanics*, 52(1):477–508, 2020.

[11] Chenyue Xie, Jianchun Wang, Hui Li, Minping Wan, and Shiyi Chen. Artificial neural network mixed model for large eddy simulation of compressible isotropic turbulence. *Physics of Fluids*, 31(8), 2019.

[12] Chenyue Xie, Jianchun Wang, Hui Li, Minping Wan, and Shiyi Chen. Spatial artificial neural network model for subgrid-scale stress and heat flux of compressible turbulence. *Theoretical and Applied Mechanics Letters*, 10(1):27–32, 2020.

[13] Maurits H Silvis, H Jane Bae, F Xavier Trias, Mahdi Abkar, and Roel Verstappen. A nonlinear subgrid-scale model for large-eddy simulations of rotating turbulent flows. *arXiv preprint arXiv:1904.12748*, 2019.

[14] Lei Yang, Dong Li, Kai Zhang, Kun Luo, and Jianren Fan. Artificial neural-network-based subgrid-scale model for large-eddy simulation of isotropic turbulence. *Physics of Fluids*, 36(7), 2024.

[15] Hugo Frezat, Guillaume Balarac, Julien Le Sommer, Ronan Fablet, and Redouane Lguensat. Physical invariance in neural networks for subgrid-scale scalar flux modeling. *Physical Review Fluids*, 6(2):024607, 2021.

[16] Chonghyuk Cho, Jonghwan Park, and Haecheon Choi. A recursive neural-network-based subgrid-scale model for large eddy simulation: application to homogeneous isotropic turbulence. *Journal of Fluid Mechanics*, 1000:A76, 2024.

[17] Rafael Borges, Monique Carmona, Bruno Costa, and Wai Sun Don. An improved weighted essentially non-oscillatory scheme for hyperbolic conservation laws. *Journal of computational physics*, 227(6):3191–3211, 2008.

[18] Marcos Castro, Bruno Costa, and Wai Sun Don. High order weighted essentially non-oscillatory weno-z schemes for hyperbolic conservation laws. *Journal of Computational Physics*, 230(5):1766–1792, 2011.

[19] Marc T Henry de Frahan, Jon S Rood, Marc S Day, Hariswaran Sitaraman, Shashank Yellapantula, Bruce A Perry, Ray W Grout, Ann Almgren, Weiqun Zhang, John B Bell, et al. Pelec: An adaptive mesh refinement solver for compressible reacting flows. *The International Journal of High Performance Computing Applications*, 37(2):115–131, 2023.

[20] Jhon Cordova, Cesar Celis, Andres Mendiburu, Luis Bravo, and Prashant Khare. Assessment of large eddy simulation (les) sub-grid scale models accounting for compressible homogeneous isotropic turbulence, 2023.

[21] Emmanuel Motheau and John Wakefield. Investigation of finite-volume methods to capture shocks and turbulence spectra in compressible flows, 2020.

[22] Thomas S Lund and EA Novikov. Parameterization of subgrid-scale stress by the velocity gradient tensor. *Annual Research Briefs, 1992*, 1993.

[23] Branko Kosović. Subgrid-scale modelling for the large-eddy simulation of high-reynolds-number boundary layers. *Journal of Fluid Mechanics*, 336:151–182, 1997.

[24] Shia-Hui Peng and Lars Davidson. On a subgrid-scale heat flux model for large eddy simulation of turbulent thermal flow. *International Journal of Heat and Mass Transfer*, 45(7):1393–1405, 2002.

[25] Maurits H Silvis, Ronald A Remmerswaal, and Roel Verstappen. Physical consistency of subgrid-

scale models for large-eddy simulation of incompressible turbulent flows. *Physics of Fluids*, 29(1), 2017.

[26] FX Trias, Firas Dabbagh, Andrei Gorobets, and C Oliet. On a proper tensor-diffusivity model for large-eddy simulation of buoyancy-driven turbulence. *Flow, Turbulence and Combustion*, 105(2):393–414, 2020.